Research paper

Fast 3D ground penetrating radar simulations for glaciers

J. Hunziker [a,*], E.C. Slob [b], J. Irving [a]

[a] *Applied and Environmental Geophysics Group, Institute of Earth Sciences, University of Lausanne, Lausanne, Switzerland*
[b] *Faculty of Civil Engineering and Geosciences, Delft University of Technology, Delft, The Netherlands*

A R T I C L E   I N F O

A B S T R A C T

Modeling ground penetrating radar (GPR) reflection data on glaciers with methods that require the discretization of the full subsurface domain is extremely computationally expensive because of the combination of a large domain size and the comparatively short wavelength of the signal. To address this issue, we build on and extend a previously proposed approach based on the assumption of a homogeneous background medium (ice) in which various scattering objects (e.g., crevasses, channels, boulders) are embedded far from each other such that multiple scattering can be ignored. The glacier bed, below which no scatterers are assumed to exist, represents the lower limit of the modeling domain. With this method, the two-way propagation of the radar waves through the ice is simulated in a semi-analytical way, whereby scattering surfaces are represented with a set of planar elements of different electric and reflective properties, allowing a wide range of objects to be simulated. As we also take the antenna radiation pattern at the air-ice interface into account, this simple algorithm is able to produce realistic 3D GPR data in a fast and memory efficient way. In this study, we validate the presented algorithm with an analytical solution for a layered model, and we simulate radar data for a model of the Otemma glacier in Switzerland featuring a realistic topography of the glacier bed and a subglacial channel.

1. Introduction

Ground Penetrating Radar (GPR) has become an increasingly popular tool in the field of glaciology (Plewes and Hubbard, 2001; Woodward and Burke, 2007; Schroeder et al., 2020). To allow for a quantitative interpretation of these data and to test hypotheses, numerical modeling tools are required. Unfortunately, grid-based modeling approaches such as, for example, finite-differences, which are usually the tools of choice for numerical simulation of GPR data, are far too computationally expensive for use with glaciological problems. This results because of the large penetration depth of the GPR signal in combination with the relatively short wavelengths involved. Indeed, in temperate ice, structures have been imaged using GPR at depths of hundreds of meters (e.g., Arcone et al., 1995; Moorman and Michel, 2000; Irvine-Fynn et al., 2006; Murray et al., 2007). Reflections from depths of up to several kilometers have been observed, for example, in Greenland (e.g., Hodge et al., 1990; Jacobel and Hodge, 1995; Keisling et al., 2014) and Antarctica (e.g., Jacobel et al., 1996, 2009; Arcone et al., 2012a,b; Christianson et al., 2012; Gillespie et al., 2017).

As a hypothetical example, let us imagine that we wish to simulate the propagation of radar waves in a small glacier domain of size $70 \times 20 \times 20$ m using the finite-difference time-domain (FDTD)

approach. To properly sample the radar waves, we require approximately ten grid points per wavelength (Giannopoulos, 1997). If we assume that the ice contains water pockets or water-filled channels, the smallest wavelength of the GPR signal would be approximately 30 cm for a 100 MHz signal. Thus, a grid size of just a few centimeters is required for the numerical modeling, which translates to a 3D mesh containing approximately 1 billion grid points. Such a mesh would lead to impractically long runtimes and would further require approximately 24 GB of memory to store the three electromagnetic field-components in double precision for just one time step.

The problem of huge spatial simulation grids can be alleviated somewhat through the use of finer subgrids in zones of shorter wavelength (e.g., where water is present), which are embedded in a coarser grid (Diamanti and Giannopoulos, 2009). However, the computational load remains rather large and, additionally, a stable interface between the grid in the ice and the subgrids discretizing the water pockets would need to be established. For all of the above reasons, grid-based numerical modeling of GPR data on glaciers is expensive and difficult.

Here, we address the above limitation and present GPR modeling software that is based on the approximation that the glacier ice can be described as homogeneous in terms of its radar propagation velocity. Reflecting interfaces within the ice and at the glacier bed

---

* Corresponding author.
  E-mail address: jurg.hunziker@unil.ch (J. Hunziker).

are then considered explicitly as scatterers within the homogeneous domain. Under these conditions, modeling can be performed in a highly computationally and memory efficient manner using Fourier methods. Note that, although similar approaches have been proposed in previous studies (Moran et al., 2003; Shakas and Linde, 2015, 2017), the corresponding computer codes were not made publicly available and lack the flexibility to handle (in a single code) (i) antennas aligned in any orientation on the ice surface with the correct radiation pattern; and (ii) a variety of different reflecting objects (i.e., point scatterers, glacier bed, subglacial channels).

In the following, we outline the theory of our developed algorithm and present a validation example comparing the code with the analytical solution for a layered subsurface model. This is followed by a more complex simulation of 3D GPR data acquired at the Otemma glacier in Switzerland, wherein realistic topography of the glacier bed and a subglacial channel are included. Finally, we discuss the efficiency and the limitations of the proposed method.

2. Theory

In the proposed algorithm, the glacier is treated as homogeneous in terms of its radar propagation velocity and is bounded by the air-ice interface on top and the glacier bed at the bottom. The assumption of a constant velocity in glacier ice is commonly made when both modeling and processing glacier GPR data (e.g., Moran et al., 2003; Egli et al., 2021), and can be generally well justified by the limited variations in ice porosity and thus water content. The body of ice can contain several objects that are assumed to be far enough from each other such that secondary scattering can be neglected without too much loss of realism. Radar pulses are emitted and received by antennas located at the surface and the corresponding radiation pattern is taken into account by analytical far-field formulations (Engheta et al., 1982). Propagation of the radar waves through the glacier ice is done in a semi-analytical way, making the gridding of the domain unnecessary. Only the surfaces of the scattering objects inside the ice and the glacier bed need to be discretized. In the case of large objects or surfaces, this is done using a multitude of small planar scattering elements, whereas small objects are represented by a single point scatterer. Each scattering element produces a response to the emitted signal. Summing up all of these responses results in the final trace that would be recorded by the GPR receiver antenna.

The following three steps are carried out in the frequency domain separately for each scatterer, planar scattering element or point scatterer: (1) Emission and propagation of the radar wave from the source antenna through the ice to the scatterer, (2) reflection of the signal at the scatterer, and (3) propagation back to the surface and reception of the signal at the receiver antenna. Note that, to increase the efficiency of the code, we combine the first and the third steps. Finally, the responses from all of the scatterers are summed and the data are multiplied with the spectrum of the GPR source-wavelet. The last step is an inverse Fourier transformation in order to obtain the final trace in the time domain. A flowchart summarizing the essential steps of the algorithm is provided in Fig. 1.

2.1. Antenna radiation pattern and wave propagation

The GPR antennas are represented in our algorithm as horizontal infinitesimal electric dipoles. As the scatterers are typically far away from the antennas in a glacial setting, neglecting the size of the antennas is a simplification that has little impact on the simulated data. The antennas are located at the air-ice interface and oriented at an arbitrary angle, whereby an angle of 0° corresponds to an orientation parallel to the x-axis. The electric field E caused by a Dirac-impulse emitted by such an antenna parallel to the x-axis is described in the far field by the expressions given by Engheta et al. (1982) and later studied by Arcone (1995). The spherical components of the electric field in the upper
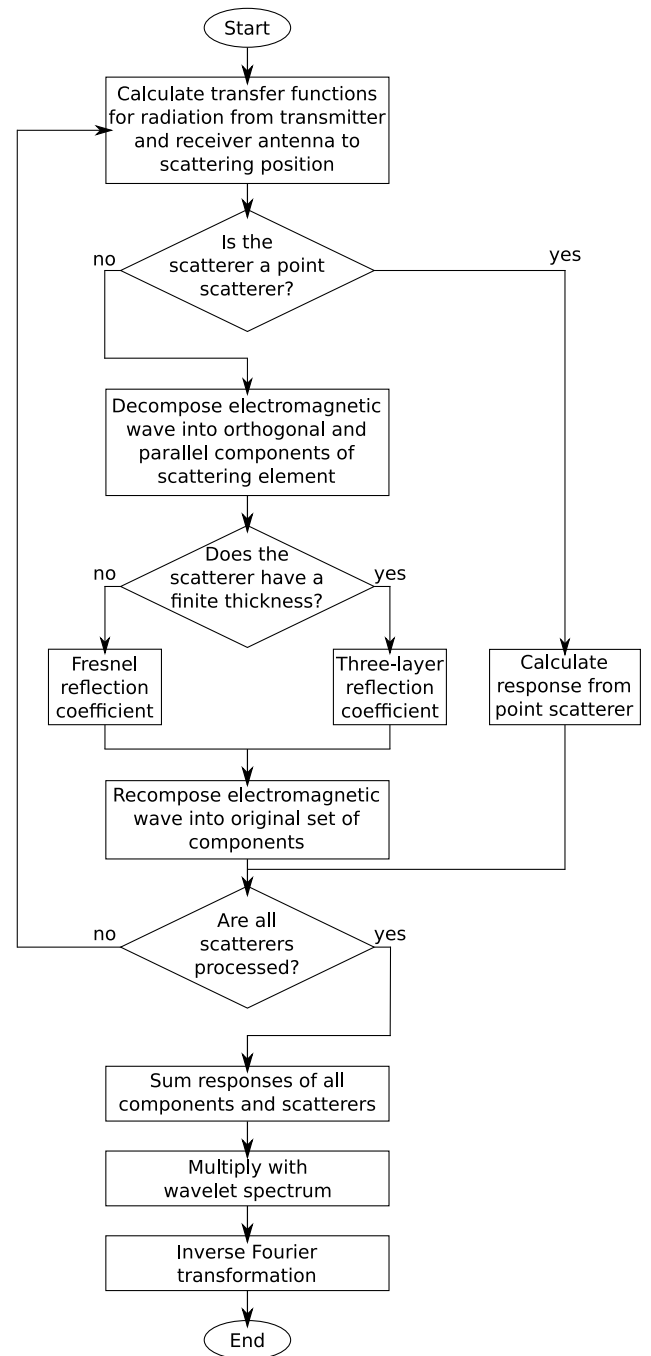

Fig. 1. Flow chart of the algorithm.

halfspace consisting of air, $E_{1,\theta}$ and $E_{1,\phi}$, are given in the frequency domain as a function of dip from the vertical (θ), horizontal azimuth measured from the negative x-axis (ϕ), and radial distance from the source (r) as

$$E_{1,\theta} = K(r)\frac{\cos\phi}{n}\left[\frac{\cos^2\theta}{\cos\theta + \sqrt{n^2 - \sin^2\theta}} - \sin^2\theta\cos\theta\frac{\cos\theta - \sqrt{n^2 - \sin^2\theta}}{n^2\cos\theta + \sqrt{n^2 - \sin^2\theta}}\right], \quad (1)$$

$$E_{1,\phi} = -\frac{K(r)}{n}\frac{\cos\theta\sin\phi}{\cos\theta + \sqrt{n^2 - \sin^2\theta}}. \quad (2)$$

As electromagnetic waves are transverse, the radial component E_r is zero. In the above equations, n is the index of refraction at the air–ice interface, which is given by

$$n = \sqrt{\frac{\varepsilon_{r,\text{ice}}}{\varepsilon_{r,\text{air}}}}, \tag{3}$$

with $\varepsilon_{r,\text{ice}}$ and $\varepsilon_{r,\text{air}}$ being the relative electric permittivity in ice and air, respectively. The factor $K(r)$ is given by

$$K(r) = \frac{iI\delta z k_m \eta e^{ik_m r}}{2\pi r}, \tag{4}$$

where $\eta = \mu_0/\sqrt{\varepsilon_0 \mu_0}$ is the electromagnetic impedance of free space with μ_0 and ε_0 being the free-space magnetic permeability and electric permittivity, respectively, $k_m = \omega\sqrt{\varepsilon_{r,m}\varepsilon_0\mu_0}$ is the vertical wavenumber in the medium having relative permittivity $\varepsilon_{r,m}$ and with ω being the angular frequency. Parameter I is the current amplitude (set to 1 A throughout this paper), δz is the dipole element length (set to 0.5 m throughout this paper), and $i = \sqrt{-1}$ is the imaginary unit. Note that the parameters I and δz are of minor importance as they only scale the overall amplitude of the radiated signal by a constant factor.

In the lower halfspace consisting of ice, the electric-field components $E_{2,\theta}$ and $E_{2,\phi}$ depend additionally on the critical angle $\theta_c = \sin^{-1}(1/n)$. For $\pi - \theta_c \le \theta \le \pi$ we have

$$E_{2,\theta} = K(r)\cos\phi \left[\sin^2\theta\cos\theta \frac{\sqrt{1 - n^2\sin^2\theta} + n\cos\theta}{n\sqrt{1 - n^2\sin^2\theta} - \cos\theta} \right.$$
$$\left. - \frac{\cos^2\theta}{\sqrt{1 - n^2\sin^2\theta} - n\cos\theta} \right], \tag{5}$$

$$E_{2,\phi} = K(r)\frac{\cos\theta\sin\phi}{\sqrt{1 - n^2\sin^2\theta} - n\cos\theta}. \tag{6}$$

For $\pi/2 \le \theta \le \pi - \theta_c$ we have

$$E_{2,\theta} = K(r)\cos\phi \left[\sin^2\theta\cos\theta \frac{\sqrt{n^2\sin^2\theta - 1} - in\cos\theta}{n\sqrt{n^2\sin^2\theta - 1} + i\cos\theta} \right.$$
$$\left. + i\frac{\cos^2\theta}{\sqrt{n^2\sin^2\theta - 1} + in\cos\theta} \right], \tag{7}$$

$$E_{2,\phi} = -iK(r)\frac{\cos\theta\sin\phi}{\sqrt{n^2\sin^2\theta - 1} + in\cos\theta}. \tag{8}$$

Eq. (1) through (8) provide the radiated electric field at a distance r from the source antenna. Note that the equations are only valid in the far field. To investigate the errors associated with the use of these expressions in the near and intermediate fields, we compare in Fig. 2 the radiation pattern obtained using Eq. (1) through (8) with the exact solution to Maxwell's equations for a point dipole on the interface of two halfspaces in the horizontal-wavenumber frequency domain, where the inverse spatial Fourier transformation is computed using numerical integration by quadratures (Slob and Fokkema, 2002). Note that the antenna radiation pattern predicted by the far-field expressions (Eq. (1) to (8)) will not change with distance from the antenna aside from a change in overall amplitude. In contrast, the shape of the radiation pattern calculated with the exact solution also changes as a function of distance r. Therefore, in Fig. 2, we plot the radiation patterns obtained with the exact solution for various distances r and normalize them to facilitate the comparison of their shapes.

We observe that the nulls appearing in the E-plane of the far-field radiation pattern around 150° and 210° do not exist in the exact solution. However, the exact solution features side lobes growing as a function of distance from the antennas proving that the far-field radiation pattern is close to the true one for large distances. The side lobes of the exact solution consist of multiple smaller side lobes, while the far-field solution shows only one clear side lobe. These multiple smaller side lobes come from the interaction between the head-wave and the spherical wave in the lower halfspace in the exact solution.

There is only one clear main side lobe in the far-field solution, because there the head-wave is not modeled.

In the H-plane, the near-field radiation is equally distributed between 120° and 240° for the exact solution, but with increasing distance from the source, radiation peaks in the ranges 120° to 150° as well as 210° to 240° form, similarly to those observed in the corresponding far-field radiation pattern.

Thus, for targets that are at least 50 m away from the antennas, the far-field radiation pattern (Fig. 2a and c) is sufficiently close to the full-field radiation pattern (Fig. 2b and d). As the targets considered in this study are indeed at least separated by 50 m from the antennas, the far-field radiation pattern is adequate enough for this study, but one should keep in mind that errors are introduced for targets close to the antennas.

2.2. Reflection coefficients

If the particular scattering object being considered is represented by a collection of small planar elements that together form the surface of the scatterer, then one of two reflection coefficients is used to calculate the reflection response. The simple Fresnel reflection coefficient is used to mimic objects that are large in volume, such as for example the bedrock at the glacier bed. It has the same formulation in the transverse electric (TE) and the transverse magnetic (TM) modes:

$$R_{\text{TE,TM}} = \frac{k_1 - k_2}{k_1 + k_2}, \tag{9}$$

where k_1 and k_2 are the vertical wavenumbers of the ice and the scatterer, respectively, where vertical refers to the direction orthogonal to the scattering element. In contrast, the three-layer reflection coefficient can be used to model objects of limited thickness, such as sediment layers or channels. It is given by Bradford and Deeds (2006):

$$R_{\text{TE}} = \frac{k_1 - k_3 - i\left(\frac{k_1 k_3}{k_2} - k_2\right)\tan(k_2 d)}{k_1 + k_3 - i\left(\frac{k_1 k_3}{k_2} + k_2\right)\tan(k_2 d)}, \tag{10}$$

$$R_{\text{TM}} = \frac{k_1\varepsilon_3 - k_3\varepsilon_1 - i\left(\frac{k_1 k_3\varepsilon_2}{k_2} - \frac{k_2\varepsilon_1\varepsilon_3}{\varepsilon_2}\right)\tan(k_2 d)}{k_1\varepsilon_3 + k_3\varepsilon_1 - i\left(\frac{k_1 k_3\varepsilon_2}{k_2} + \frac{k_2\varepsilon_1\varepsilon_3}{\varepsilon_2}\right)\tan(k_2 d)}, \tag{11}$$

where k_1, k_2, and k_3 refer to the vertical wavenumbers of the ice, the scatterer, and the medium below the scatterer, respectively, and ε_1, ε_2, and ε_3 refer to the electric permittivities of these three media. For an object embedded in the ice, $k_1 = k_3$ and $\varepsilon_1 = \varepsilon_3$. To model the glacier bed with a sediment layer between the ice and the bedrock, the subscripts 1, 2, and 3 would refer to the ice, the sediment layer, and the bedrock, respectively. The thickness of the middle layer is represented by the variable d.

Before the reflection coefficient can be applied, the three orthogonal components of the electromagnetic wave, E_θ, E_ϕ, and E_r, must be expressed in terms of three different orthogonal components such that two of these components are parallel and the third one orthogonal to the scattering element under consideration. The parallel components are then multiplied with the TE-mode reflection coefficient, while the orthogonal component is multiplied with the TM-mode reflection coefficient.

2.3. Point scatterers

We represent small objects inside the ice as point scatterers instead of as planar scattering elements. To this end, we use the analytical expression for the wavefield scattered by a point-like disturbance of the background electric permittivity given by Saintenoy and Tarantola (2001):

$$\mathbf{E} = \ln\left(\frac{\varepsilon_{\text{ps}}}{\varepsilon_1}\right)\frac{V}{4\pi r_{\text{rec}}v^2}\left[\hat{\mathbf{r}}_{\text{rec}} \times \left(-\omega^2\right)\mathbf{E}_{\text{inc}}\right] \times \hat{\mathbf{r}}_{\text{rec}}, \tag{12}$$

a) Engheta et al. (1982), E-plane (xz-plane)

b) Slob and Fokkema (2002), E-plane (xz-plane)

c) Engheta et al. (1982), H-plane (yz-plane)
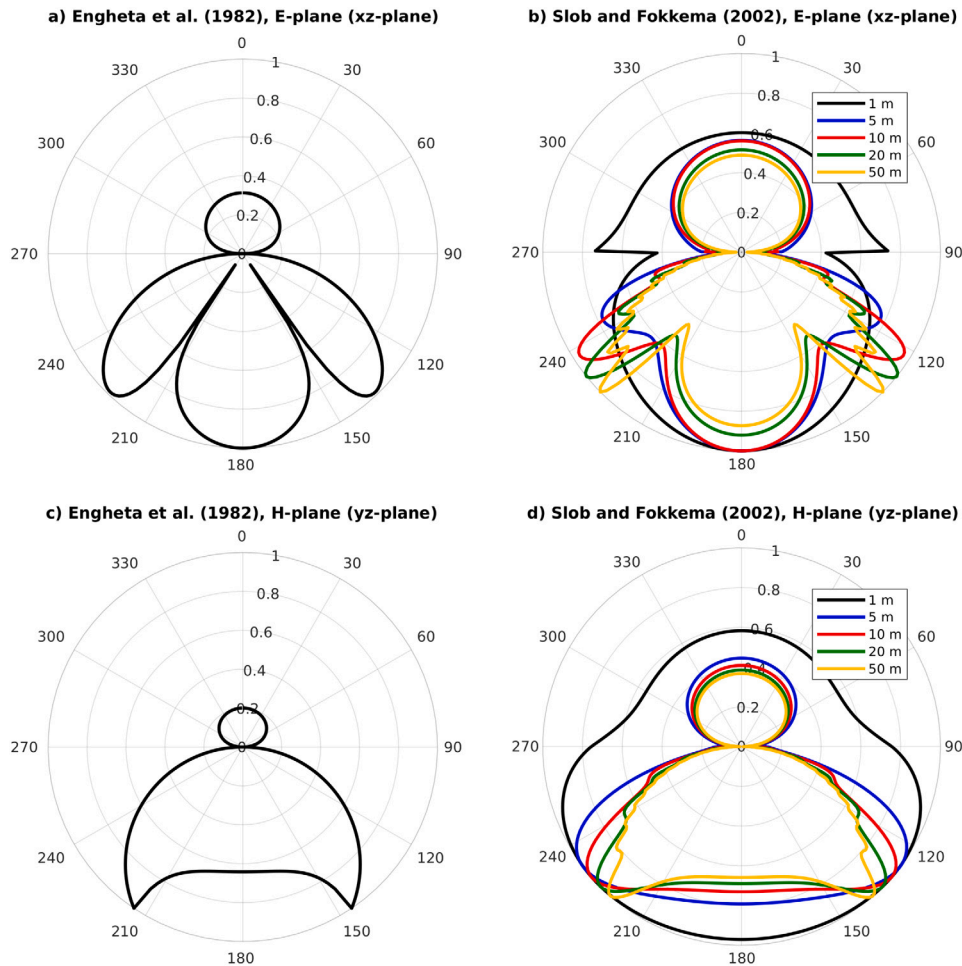
d) Slob and Fokkema (2002), H-plane (yz-plane)

Fig. 2. Radiation patterns for a dipole antenna oriented parallel to the x-axis. Above the horizontal axis (90° - 270° line), radiation into the air is shown, while the lower part depicts radiation into the ice ($\varepsilon_r = 3.2$). Each plot has been normalized to allow for a comparison regardless of distance from the source. The analytical radiation pattern used in this paper (Engheta et al., 1982; Arcone, 1995) is shown in (a) and (c), and the radiation pattern based on the exact solution of Maxwell's equations (Slob and Fokkema, 2002) is shown for various distances from the antennas in (b) and (d). Note that the analytical far-field solution does not change shape as a function of distance from the source. (a) and (b) show the radiation patterns in the E-plane or xz-plane and (c) and (d) show the radiation patterns in the H-plane or yz-plane.

where bold quantities represent three-component vectors, ε_{ps} is the electric permittivity of the point scatterer, V is its volume, r_{rec} is the distance between the point scatterer and the receiver antenna, v is the velocity of the electromagnetic wave in ice, $\hat{\mathbf{r}}_{rec}$ is the unit vector pointing from the point scatterer to the receiver antenna, and $\mathbf{E}_{inc}$ is the incident electric field vector at the point scatterer in Cartesian coordinates, and $\mathbf{E}$ is the scattered field vector.

Note that Eq. (12) gives the scattered electric field vector $\mathbf{E}$ at the location of the point scatterer. To obtain the response of the point scatterer at the receiver location, $\mathbf{E}$ needs to be propagated to the corresponding position at the surface. In our implementation, this is carried out in conjunction with the calculation of the radiation pattern of the receiver antenna described in the previous subsection.

2.4. Wavelet

After propagation and reflection, the response of all of the scatterers is summed to obtain the complete GPR trace in the frequency domain. Before applying the inverse Fourier transformation to obtain the time-domain trace, the frequency spectrum of the signal is multiplied with the spectrum of the GPR source wavelet W.

For all of the examples shown in this paper, we consider a source wavelet equal to the double derivative of a Gaussian function having a center frequency of 100 MHz and a time shift of 12 ns to ensure causality. However, any other function could be considered.
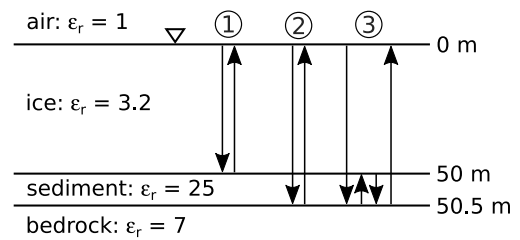

Fig. 3. Subsurface model for the validation of the FROGS code (not to scale). The inverted triangle indicates the depth of the GPR antennas and the arrows represent the ray paths of the three events shown in Fig. 4.

3. Validation

Our implementation of the algorithm described in the previous section is available on github as a MATLAB package. We call our code "Fast Radar-On-Glacier Simulation" or, for short, "FROGS".

In this section, we present a validation of the code, where we compare the results obtained with FROGS with those corresponding to a semi-analytical solution for a layered Earth (Hunziker et al., 2015; Werthmüller, 2017). The considered subsurface model consists of an infinite, horizontal plane at 50.5 m depth that could be considered to be
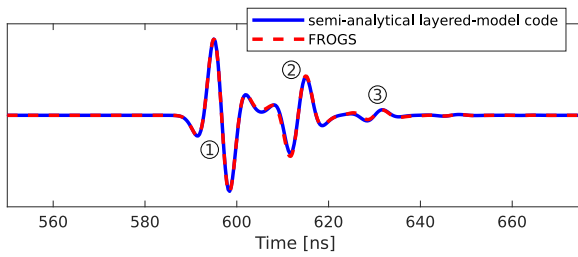
Fig. 4. Comparison of results obtained using the FROGS code with those obtained using the semi-analytical solution for the layered model shown in Fig. 3. A three-layer reflection coefficient was used in FROGS to simulate the sediment layer on top of the bedrock. The labeled events are ① the reflection from the top of the sediment layer, ② the reflection from the top of the bedrock, and ③ an internal multiple reflection inside the sediment layer. The ray paths of these events are graphically depicted in Fig. 3.

Fig. 5. Topography of the Otemma glacier bed with the hypothetical position of a channel in red and the outline of the simulated 3D GPR survey in black.

bedrock. This plane is covered by a 0.5 m thick layer of sediments. The colocated GPR antennas are placed on the ice surface at 0 m depth. A sketch of the model and the corresponding relative electric permittivity values is shown in Fig. 3.

In FROGS, we represent the infinite horizontal plane of scattering elements as a circle of radius of 20 m and place the GPR antennas at the center of the circle, 50 m above the plane. The circle is discretized into 5024 scattering elements of size 0.5×0.5 m. Note that, as we use the three-layer reflection coefficient, we only need one plane of scattering elements to represent both, the sediment surface at 50 m depth and the bedrock surface at 50.5 m depth.

In Fig. 4 we compare the GPR traces obtained using the analytical solution with those obtained using the FROGS numerical modeling code. We see that the results are identical, which confirms that use of expressions (1) through (8) is fully appropriate for this example. Three events can be seen on these traces, which are the reflection from the top of the sediment layer (event ① in Figs. 3 and 4), the reflection from the top of the bedrock (event ②) and an internal reflection inside the sediment layer (event ③).

Note that, for the example shown in Fig. 3, a surface multiple should normally appear in the GPR trace at approximately twice the travel time of the bedrock reflection, which is beyond the time limits of the plot shown in Fig. 4. While FROGS correctly accounts for multiple reflections inside the sediment layer through the use of the three-layer reflection coefficient, it will not reproduce this surface-based multiple. The semi-analytical solution, on the other hand, correctly accounts for this behavior.

4. Example

In order to show the capabilities of FROGS in a more realistic context, we use the code to simulate 3D GPR data that would be acquired over a glacier bed containing a subglacial meltwater-channel. Our example is based on the Otemma glacier in the canton of Wallis in Switzerland. In this regard, we obtained the topography of the glacier bed from the 2020 release of the Swiss Glacier Thickness database (Grab et al., 2021) and the position of a channel from Egli et al. (2021), who considered the Shreve potential for fully pressurized flow to calculate the theoretically most likely flow path near the glacier snout. We set the channel to be four meters wide and its cross-section to be a semicircle with a maximum height of two meters. The topography of the glacier bed in the area of interest is shown in Fig. 5. Superimposed are the position of the channel (red) and the area in which the 3D GPR simulation was conducted (black).

For the simulation, we positioned the GPR antennas at a constant elevation of 2700 m, approximately 200 m above the glacier bed. A total of 89 lines were simulated, which oriented north-west to south-east. Each line consisted of 85 antenna positions. The spacing in in-line direction as well as in the cross-line direction was 0.5 m, meaning that
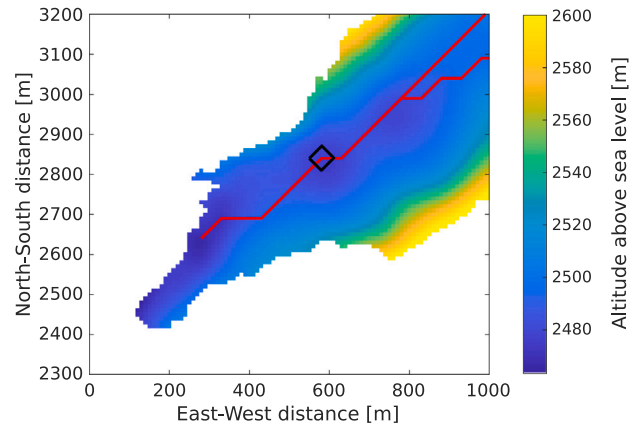
a rectangular region of 42×44 m was modeled. Considering the typical size of a glaciological domain of interest, the chosen area is relatively small. This allows for a fast reproduction of our results by readers and is at the same time sufficient to demonstrate the capabilities of the code. The antennas were oriented orthogonal to the line direction and the source and the receiver antennas were colocated.

If data are to be simulated close to the edge of the glacier, the region outside of the defined glacier bed (in white in Fig. 5) must be filled with topographic data to avoid boundary effects. In this regard, we propose to fill each empty pixel with the same value as at the edge of the glacier bed at the same north–south distance and smooth the result with a convolutional filter.

The resulting topographic data were divided into 26.5 million scattering elements of size 0.3×0.3 m. Calculating the response for all of these elements in FROGS is unnecessarily time consuming, as scattering elements far away from the source and the receiver antennas do not influence the resulting data. For this reason, we decided to ignore all scattering elements that were more than 200 m laterally away from the antennas. To avoid boundary effects, the responses between 190 and 200 m lateral distance from the antennas were gradually weighted to have lesser importance before being summed to obtain the final trace.

To model the glacier bed, the simple Fresnel reflection coefficient between ice ($\varepsilon_r = 3.2$) and bedrock ($\varepsilon_r = 7$) was used. At the location of the subglacial channel, the three-layer reflection coefficient was used with a layer of water ($\varepsilon_r = 81$) between the ice and the bedrock.

A horizontal and a vertical slice through the simulated data are shown in Figs. 6a and 6d, respectively. Note that the time range of the vertical slice is focused only upon the region of the data containing the glacier bed reflection. To isolate the effect of the channel, we also simulated data without the channel (Figs. 6b and 6e). Subtracting the dataset without the channel from the dataset containing the channel resulted in the response of the channel alone (Figs. 6c and 6f).

We observe that the glacier bed produces a strong reflection including the typical tripling or bow-tie structure of the reflection caused by the valley topography at around 30 m inline distance in Fig. 6e. The channel is seen as a diffraction hyperbola, which is broad due to the large vertical distance between the GPR antennas and the channel (Fig. 6f). The top and bottom of the channel produce two strong single reflections as well as several weaker reflections due to reverberations of the electromagnetic waves inside the channel (below 2650 ns in Fig. 6f).

In the horizontal slices (Figs. 6a and 6c), the channel is visible as two tails of the corresponding diffraction hyperbola. The distance between the two tails varies as the topography is not flat at the glacier bed. The superimposed red line showing the position of the channel lies in the middle between the two tails.
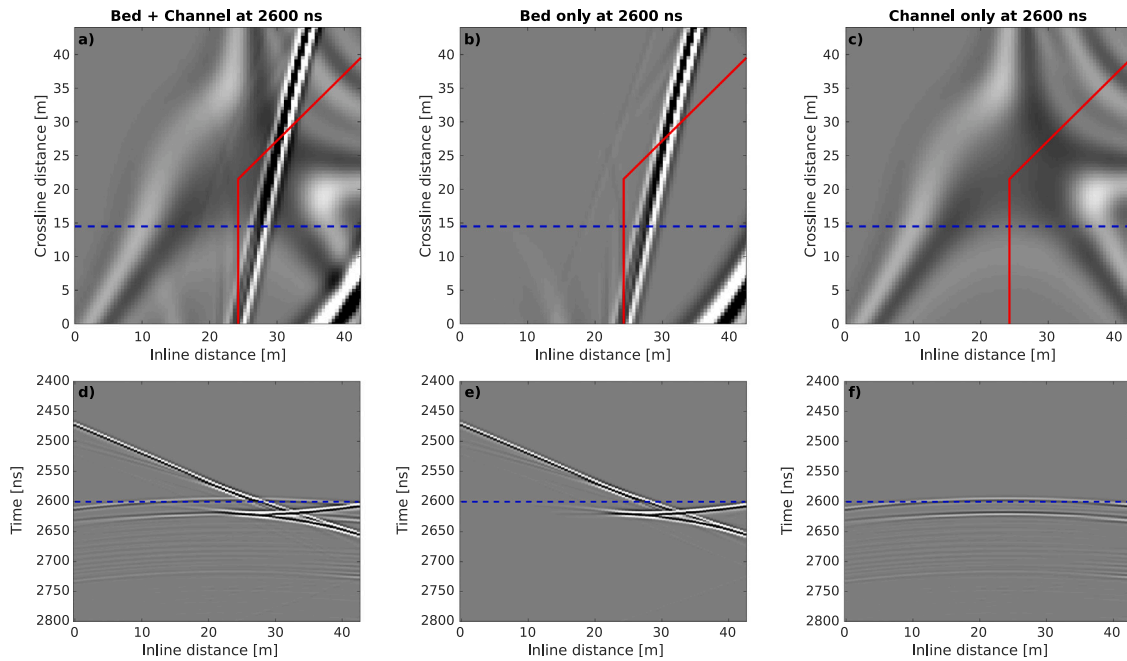
Fig. 6. Simulated data above the area indicated by the black rectangle in Fig. 5. Subfigures (a) to (c) are time slices at 2600 ns and subfigures (d) to (f) are vertical cross-sections along the line measured at 14.5 m. a) and (d) contain the reflections from the glacier bed as well as from the channel, (b) and (e) contain only the reflections from the glacier bed, and (c) and (f) only the reflections from the channel. The red lines show the position of the channel and the blue dashed lines show the position of the intersections between the time slices (a) to (c) and the vertical slices (d) to (f).

Note that, to accurately simulate a single GPR trace with a finite-difference code using the geometry considered in this example, we would require a domain size of 400 × 400 × 240 m to capture all reflections that can arrive at the antenna and a spatial discretization of 2.5 × 2.5 × 2.5 cm. This corresponds to a memory demand of 172 TB, which is far greater than the computer resources available to us at the time of writing. This illustrates that FROGS has a clear place on the spectrum of GPR numerical modeling methods, opening the possibility for simulation for certain 3D domains where traditional methods will fail.

5. Discussion

5.1. Runtime

For the validation example presented in Section 3, FROGS needed 2.7 s to compute the red dashed trace shown in Fig. 4 on a laptop machine containing an Intel i7-4600M CPU at 2.90 GHz. For the Otemma glacier example, which features roughly 5000 times more scattering elements, FROGS, parallelized over the scattering elements, needed 9304 s to calculate the response of 85 antenna positions (excluding the time required for the parametrization of the glacier bed) on our dated computer cluster using 32 AMD Opteron 6136 processors at 0.8 GHz. This amounts to 110 s per antenna position. Instead of parallelizing FROGS over the scattering elements, parallelization of the code across the antenna positions may be more computationally efficient when the number of antenna positions is large.

Concerning the runtime of FROGS, one should be aware that it is greatly affected by the complexity of the subsurface domain to be modeled, but not by the domain size. If more scattering elements are required for a simulation, the runtime will increase even though the domain size remains the same. On the other hand, if the subsurface domain can be represented with a rather small number of scattering elements, the runtime will be low even though the size of the overall domain is large. This is in contrast to a grid-based numerical modeling approach, for which the runtime will always increase with increasing domain size.

5.2. Size of scattering elements

The size of the scattering elements is an important parameter for efficient simulations as making the elements bigger allows for a reduction of their number and, thus, a reduction in computational time. To assess the optimal size of the scattering elements for the validation example presented earlier, we run the example for scattering elements having side lengths of 1, 2, 4 and 6 m. The resulting traces are plotted in Fig. 7. Note that the red trace plotted in each subfigure corresponds to a side length of $l = 0.5$ m and is identical to the red dashed trace depicted in Fig. 4.

The results in Fig. 7 show that, for this example, a side length of 1 m yields an equally acceptable result as a side length of 0.5 m (Fig. 7a). Doubling the side length reduces the runtime on the first author's laptop from 2.7 s to 1 s. We see that increasing the side length of the scattering elements to 2 or 4 m introduces high-amplitude oscillations behind the first arrival (Figs. 7b and 7c), which result from imperfect interference of the responses produced by the different scattering elements. Note that the reflection from the top of the sediment layer is still correct in these cases, whereas using a side length of 6 m (Fig. 7d) also affects this arrival.

As we expect the optimal size of the scattering elements to vary as a function of the distance between the target and the GPR antennas, as well as the topography of a reflector, such an experiment as outlined here should be carried out before FROGS simulations are performed in order to find the optimal value for this parameter.

5.3. Assumptions and limitations

Behind our efficient algorithm are several simplifications that warrant further discussion. First of all, we assume that the sampled medium can be described as a homogeneous domain containing several scattering objects that are far enough away from each other and from the surface to make the effects of multiple scattering negligible. As we aim to use this algorithm to simulate GPR data on glaciers, such as in the Alps or on large ice masses such as on Antarctica, the assumption of a homogeneous background medium appears to be rather
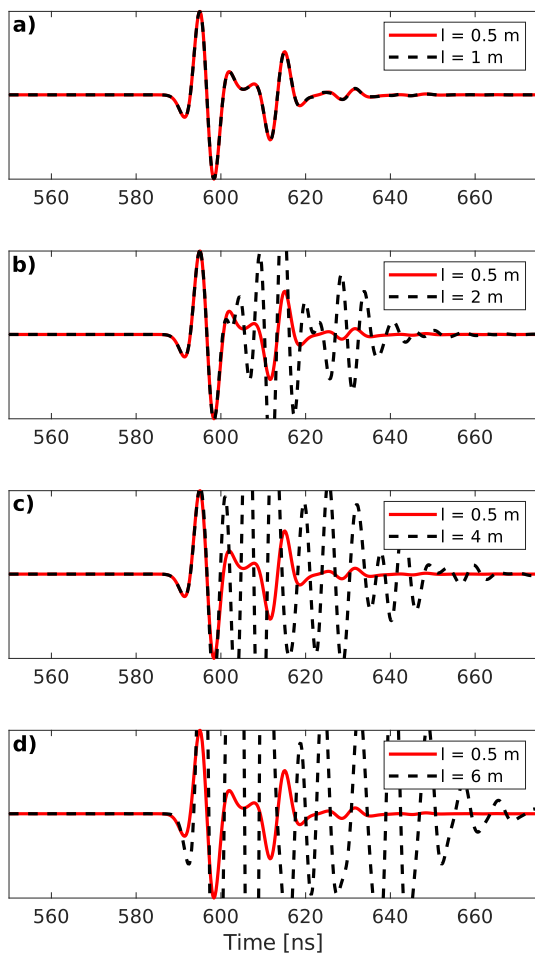
Fig. 7. The trace from the validation example recalculated for side lengths of (a) $l = 1$ m, (b) $l = 2$ m, (c) $l = 4$ m and (d) $l = 6$ m (black trace). The red trace is the same as the red dashed trace in Fig. 4, which corresponds to a side length of $l = 0.5$ m.

well fulfilled. If necessary, one could extend the algorithm to include smooth vertical changes in GPR velocity as a function of, for example, ice density through the adjustment of the vertical wavenumber in the wave propagation.

The second assumption, that the objects embedded in the ice need to be far enough from each other and the surface, expresses itself in the complete absence of secondary scattering in our simulations. This means that an event, which is registered at the receiver after the GPR pulse has been reflected first from one object and then from another, will be absent in the FROGS output. In the same way, surface multiples, which are events that are reflected twice in the subsurface with a reflection at the air–ice interface in between before being recorded, will also be absent. To our knowledge, such secondary scattering is rather rare in GPR data, as evidenced by the great success of single-scattering-based algorithms for the processing and analysis of GPR data (Irving et al., 2009; Schmelzbach et al., 2012; Xu et al., 2020, 2021; Liu et al., 2022).

However, not all multiple scattering is neglected in FROGS. As seen in the validation example, use of a three-layer reflection coefficient allows for multiple scattering within a layer. In a similar way, waveguides can be simulated with the FROGS algorithm if they can be represented as a layer. To study these phenomena in more complex settings, finite-difference algorithms or comparable approaches are necessary.

We further assume that the electrical conductivity can be neglected in the FROGS code. This is generally well justified for ice, but not so

for rocks or sediments. Therefore, when using the three-layer reflection coefficient to simulate, for example, a layer of sediments on top of the glacier bed, one needs to be aware that no attenuation due to the electrical conductivity of the material will be taken into account. Thus, the sediment layer will cause more multiples in the data simulated by FROGS than in reality. This could be mitigated by extending FROGS to use a three-layer reflection coefficient that allows for a non-zero electric conductivity in the sandwiched layer.

Anisotropy in the background medium, in our case ice, is also neglected. Therefore, effects caused by preferential orientation of ice crystals (Kovacs and Morey, 1978) or effects related to changes in the ice related to the orientation of crevasses (Nobes, 1999) cannot be simulated in FROGS. However, apparent anisotropic effects due to the orientation of the antennas relative to reflectors (Nobes and Annan, 2000) are taken into account through use of the complete far-field radiation pattern.

All of the simulations presented in this paper assumed the ice surface to be flat, but surface topography may be easily considered with the FROGS code in the sense that the ice surface is defined to be at the vertical position of the GPR antennas and the algorithm allows us to place the antennas anywhere in space. However, the implemented radiation pattern assumes a locally flat, horizontal surface. Therefore, the simulated data may be affected by some artifacts if a highly complex surface topography is present.

As one of the first steps in GPR processing is the removal of the direct wave between the transmitter and receiver antennas, we have decided not to include this event in the data simulated with the FROGS algorithm. In contrast, finite-difference algorithms do simulate the direct wave. If desired, the direct wave could easily be included by evaluating the electric field generated by the radiation pattern directly at the receiver antenna instead of at the location of the scatterers.

Due to its speed and its flexibility of incorporating different types of scattering, FROGS represents a highly useful tool for exploring various subsurface models to help interpret GPR field data or to design optimal measurement campaigns before going to the field. However, if one of the assumptions outlined above is violated, additional, possibly expensive, simulations with a finite-difference code should be considered in order to avoid erroneous data interpretations.

6. Conclusions

We have presented an algorithm for the numerical modeling of GPR data in a fast and memory-efficient way. It is particularly well suited to glaciological acquisitions over large domains, because its runtime depends on the complexity of the subsurface domain and not its size, which is usually huge in glaciological studies due to the large penetration depth of electromagnetic waves in ice. Further, the assumption that scattering objects are far from each other and embedded in a homogeneous background medium is not unrealistic in most glaciological settings.

Computer code availability

The presented algorithm is available on https://github.com/jhunziker/FROGS as a MATLAB package and on https://github.com/jhunziker/FROGS_cpp as a Python/C++ package.

CRediT authorship contribution statement

J. Hunziker: Methodology, Investigation, Software, Writing – original draft. **E.C. Slob:** Software, Investigation, Supervision. **J. Irving:** Conceptualization, Project administration, Writing – review & editing.

Declaration of competing interest

The authors declare that they have no known competing financial interests or personal relationships that could have appeared to influence the work reported in this paper.

Data availability

All data used are already publicly available.

Acknowledgments

We thank Alexis Shakas for sharing his code with us and Antonios Giannopoulos for insightful discussions about antenna radiation patterns. We also thank David Nobes and an anonymous reviewer as well as the associate editor Leonardo Azevedo for their comments.

References

Arcone, S.A., 1995. Numerical studies of the radiation patterns of resistively loaded dipoles. J. Appl. Geophys. 33, 39–52.

Arcone, S.A., Jacobel, R., Hamilton, G., 2012a. Unconformable stratigraphy in East Antarctica: Part I. Large firn cosets, recrystallized growth, and model evidence for intensified accumulation. J. Glaciol. 58, 240–252.

Arcone, S.A., Jacobel, R., Hamilton, G., 2012b. Unconformable stratigraphy in East Antarctica: Part II. Englacial cosets and recrystallized layers. J. Glaciol. 58, 253–264.

Arcone, S.A., Lawson, D.E., Delaney, A.J., 1995. Short-pulse radar wavelet recovery and resolution of dielectric contrasts within englacial and basal ice of Matanuska Glacier, Alaska, U.S.A. J. Glaciol. 41, 68–86.

Bradford, J.H., Deeds, J.C., 2006. Ground-penetrating radar theory and application of thin-bed offset-dependent reflectivity. Geophysics 71, K47–K57.

Christianson, K., Jacobel, R.W., Horgan, H.J., Anandakrishnan, S., Alley, R.B., 2012. Subglacial Lake Whillans - Ice-penetrating radar and GPS observations of a shallow active reservoir beneath a West Antarctic ice stream. Earth Plan. Sci. Lett. 331–332, 237–245.

Diamanti, N., Giannopoulos, A., 2009. Implementation of ADI-FDTD subgrids in ground penetrating radar FDTD models. J. Appl. Geophys. 67, 309–317.

Egli, P.E., Irving, J., Lane, S.N., 2021. Characterization of subglacial marginal channels using 3-D analysis of high-density ground-penetrating radar data. J. Glaciol. 67 (264), 759–772. http://dx.doi.org/10.1017/jog.2021.26.

Engheta, N., Papas, C.H., Elachi, C., 1982. Radiation patterns of interfacial dipole antennas. Radio Sci. 17, 1557–1566.

Giannopoulos, A., 1997. The Investigation of Transmission-Line Matrix and Finite-Difference Time-Domain Methods for the Forward Problem of Ground Probing Radar (Ph.D. thesis). The University of York.

Gillespie, M.K., Lawson, W., Rack, W., Anderson, B., Blankenship, D.D., Young, D.A., Holt, J.W., 2017. Geometry and ice dynamics of the Darwin-Hatherton glacial system, Transantarctic Mountains. J. Glaciol. 63 (242), 959–972. http://dx.doi.org/10.1017/jog.2017.60.

Grab, M., Mattea, E., Bauder, A., Huss, M., Rabenstein, L., Hodel, E., Linsbauer, A., Langhammer, L., Schmid, L., Church, G., Hellmann, S., Délèze, K., Schaer, P., Lathion, P., Farinotti, D., Maurer, H., 2021. Ice thickness distribution of all Swiss glaciers based on extended ground penetrating radar data and glaciological modeling. J. Glaciol. http://dx.doi.org/10.3929/ethz-b-000434697.

Hodge, S.M., Wright, D.L., Bradley, J.A., Jacobel, R.W., Skou, N., Vaughn, B., 1990. Determination of the surface and bed topography in central greenland. J. Glaciol. 36, 17–30.

Hunziker, J., Thorbecke, J., Slob, E., 2015. The electromagnetic response in a layered vertical transverse isotropic medium: A new look at an old problem. Geophysics 80 (1), F1–F18. http://dx.doi.org/10.1190/geo2013-0411.1.

Irvine-Fynn, T.D.L., Moorman, B.J., Williams, J.L.M., Walter, F.S.A., 2006. Seasonal changes in ground-penetrating radar signature observed at a polythermal glacier, Bylot Island, Canada. Earth Surf. Process. Landf. 31, 892–909.

Irving, J., Knight, R., Holliger, K., 2009. Estimation of the lateral correlation structure of subsurface water content from surface-based ground-penetrating radar reflection images. Water Resour. Res. 45.

Jacobel, R.W., Hodge, S.M., 1995. Radar internal layers from the Greenland summit. Geophys. Res. Lett. 22, 587–590.

Jacobel, R.W., Scambos, T.A., Raymond, C.F., Gades, A.M., 1996. Changes in the configuration of ice stream flow from the West Antarctic Ice Sheet. J. Geophys. Res. 101, 5499–5504.

Jacobel, R.W., Welch, B.C., Osterhouse, D., Pettersson, R., MacGregor, J.A., 2009. Spatial variation of radar-derived basal conditions on Kamb Ice Stream, West Antarctica. Ann. Glaciol. 50, 10–16.

Keisling, B.A., Christianson, K., Alley, R.B., Peters, L.E., Christian, J.E.M., Anandakrishnan, S., Riverman, K.L., Muto, A., Jacobel, R.W., 2014. Basal conditions and ice dynamics inferred from radar-derived internal stratigraphy of the Northeast Greenland ice stream. Ann. Glaciol. 55, 127–137.

Kovacs, A., Morey, R.M., 1978. Radar anisotropy of sea ice due to preferred azimuthal orientation of the horizontal c axes of ice crystals. J. Geophys. Res. 83, 6037–6046.

Liu, Y., Irving, J., Holliger, K., 2022. High-resolution velocity estimation from surface-based common-offset GPR reflection data. Geophys. J. Int. 230, 131–144.

Moorman, B.J., Michel, F.A., 2000. Glacial hydrological system characterization using ground-penetrating radar. Hydrol. Process. 14, 2645–2667.

Moran, M.L., Greenfield, R.J., Arcone, S.A., 2003. Modeling GPR radiation and reflection characteristics for a complex temperate glacier bed. Geophysics 68, 559–565.

Murray, T., Booth, A., Rippin, D.M., 2007. Water-content of glacier-ice: Limitations on estimates from velocity analysis of surface ground-penetrating radar surveys. J. Environ. Eng. Geophys. 12, 87–99.

Nobes, D.C., 1999. The directional dependence of the Ground Penetrating Radar response on the accumulation zones of temperate Alpine glaciers. First Break 17, 249–259.

Nobes, D.C., Annan, A.P., 2000. "Broadside" versus "end-fire" radar response: Some simple illustrative examples. In: Eighth Intl. Conference on Ground Penetrating Radar. Vol. 4084. SPIE, pp. 696–701.

Plewes, L.A., Hubbard, B., 2001. A review of the use of radio-echo sounding in glaciology. Progr. Phys. Geogr. 25, 203–236.

Saintenoy, A.C., Tarantola, A., 2001. Ground-penetrating radar: Analysis of point diffractors for modeling and inversion. Geophysics 66, 540–550.

Schmelzbach, C., Tronicke, J., Dietrich, P., 2012. High-resolution water content estimation from surface-based ground-penetrating radar reflection data by impedance inversion. Water Resour. Res. 48.

Schroeder, D.M., Bingham, R.G., Blankenship, D.D., Christianson, K., Eisen, O., Flowers, G.E., Karlsson, N.B., Koutnik, M.R., Paden, J.D., Siegert, M.J., 2020. Five decades of radioglaciology. Ann. Glaciol. 61, 1–13.

Shakas, A., Linde, N., 2015. Effective modeling of ground penetrating radar in fractured media using analytic solutions for propagation, thin-bed interaction and dipolar scattering. J. Appl. Geophys. 116, 206–214.

Shakas, A., Linde, N., 2017. Apparent apertures from ground penetrating radar data and their relation to heterogeneous aperture fields. Geophys. J. Int. 209, 1418–1430.

Slob, E.C., Fokkema, J.T., 2002. Interfacial dipoles and radiated energy. Subsurf. Sens. Technol. Appl. 3, 347–367.

Werthmüller, D., 2017. An open-source full 3D electromagnetic modeler for 1D VTI media in Python: empymod. Geophysics 82 (6), WB9–WB19. http://dx.doi.org/10.1190/geo2016-0626.1.

Woodward, J., Burke, M.J., 2007. Applications of ground-penetrating radar to glacial and frozen materials. J. Environ. Eng. Geophys. 12, 69–85.

Xu, Z., Irving, J., Lindsay, K., Bradford, J., Zhu, P., Holliger, K., 2020. Estimation of the 3D correlation structure of an alluvial aquifer from surface-based multi-frequency ground-penetrating radar reflection data. Geophys. Prospect. 68, 678–689.

Xu, Z., Irving, J., Liu, Y., Zhu, P., Holliger, K., 2021. Conditional stochastic inversion of common-offset GPR reflection data. Geophysics 86, WB89–WB99.